Boundary effects on behaviour of granular material during plane strain compression

Jacek Tejchman, Wei Wu

Title: Boundary effects on behaviour of granular material during plane strain compression

Authors: Jacek Tejchman, Wei Wu

PII: S0997-7538(09)00092-8

DOI: 10.1016/j.euromechsol.2009.07.004

Reference: EJMSOL 2536

To appear in: *European Journal of Mechanics / A Solids*

Received Date: 13 March 2009

Accepted Date: 18 July 2009

Please cite this article as: Tejchman, J., Wu, W. Boundary effects on behaviour of granular material during plane strain compression, European Journal of Mechanics / A Solids (2009), doi: 10.1016/j.euromechsol.2009.07.004

Boundary effects on behaviour of granular material during plane strain compression

Jacek Tejchman[1] and Wei Wu[2]

[1]*Faculty of Civil and Environmental Engineering, Gdansk University of Technology, Gdansk, Poland, e-mail: tejchmk@pg.gda.pl*

[2]*Institut für Geotechnik, Universität für Bodenkultur, Vienna, Austria,e-mail: wei.wu@boku.ac.at*

Abstract

The paper investigates the boundary effect on the behaviour of granular materials during plane strain compression using finite element method. A micro-polar hypoplastic constitutive model was used. The numerical calculations were carried out with different initial densities and boundary conditions. The behaviour of initially dense, medium dense and loose sand specimen with very smooth or very rough horizontal boundary was investigated. The formation of shear zones gave rise to different global and local stress and strain. Comparisons of the mobilized internal friction, dilatancy and non-coaxiality between global and local quantities were made.

Keywords: boundary roughness, finite element method, micro-polar hypoplasticity, non-coaxiality, plane strain compression, shear localization, void ratio

1. Introduction

Our knowledge on the mechanical behavior of granular materials is largely based on element tests with uniform stress and homogeneous strain. Some important parameters can be obtained from the element tests such as internal friction angle and dilatancy angle (Vardoulakis 1980, Yoshida et al. 1994, Desrues et al. 1996). However, the parameters are determined with the aid of measurements of global (exterior) quantities at specimen boundaries (force and displacement), which may differ from their local quantities inside the material (impossible to be measured). These differences are caused by localized deformation in shear zones and the imperfect boundaries of specimen in laboratory tests. The effect of localized deformation and boundary conditions is important to differentiate between material behavior from structural behavior.

This paper presents some numerical simulations into the effect of localized deformation and boundary conditions during plane strain compression. The finite element method was used with a micro-polar hypoplastic constitutive model. This boundary effect was estimated by comparing the evolutions of the global and local mobilized friction, dilatancy and non-coaxiality. A uniform distribution of the initial void of sand was assumed. Our previous numerical study showed that a stochastic distribution of void ratio had only minor effect on the numerical results (Tejchman and Górski 2008). Three initial densities were studied, i.e. initially dense, medium dense and loose specimens. The lateral pressure was assumed to be constant. The horizontal boundaries were assumed to be either very smooth or very rough. The former represents ideal boundary conditions, while the latter stands for imperfect boundary conditions. Obviously, the real boundaries in the element tests are likely to be in between. This papers continues our previous study (Tejchman and Wu 2009a), where non-coaxiality and dilatancy have been investigated.

Throughout the paper, tensor notations are used. Summation over repeated indices is assumed. A superposed circle denotes an objective time derivation and a superposed dot denotes the material time derivation. Compressive stress and shortening strain are taken as negative. As a consequence, contractancy is negative and dilatancy is positive.

2. Micro-polar hypoplastic model

Non-polar hypoplastic constitutive models (Gudehus 1996, Bauer 1996, von Wolffersdorff 1996) describe the evolution of the effective stress tensor as a non-linear tensorial function of the current void ratio, stress state and rate of deformation. The non-linear tensorial functions can be formulated according to the representation theorem (Wang 1970). These constitutive models were formulated by considering the essential properties of granular materials undergoing homogeneous deformation. Hypoplastic models are capable of describing some salient properties of granular materials, e.g. non-linear stress-strain relationship, dilatant and contractant behaviour, pressure dependence, density dependence and material softening. A further feature of hypoplastic models is the inclusion of critical states, in which deformation may occur continuously at constant stress and volume. In contrast to elasto-plastic models, the following assumptions are not necessary: decomposition of deformation into elastic and plastic parts, yield surface, plastic potential, flow rule. Moreover, neither coaxiality, i.e. coincidence of principal axes of stress and principal plastic strain increments nor stress-dilatancy rule are not assumed in advance (Tejchman and Wu 2009a). The hallmark of the hypoplastic models is their simple formulation and procedure for determining the

parameters with standard laboratory experiments. The material parameters are related to granulometric properties, viz. size distribution, shape, angularity and hardness of grains (Herle and Gudehus 1999, Rondón 2007). A further advantage lies in the fact that one single set of material parameters is valid for wide range of pressure and density. The hypoplastic models have been extended to increase the application range, small strain (Niemunis and Herle 1997), anisotropy (Tejchman and Bauer 2007), and viscosity (Niemunis 2003, Gudehus 2006, Tejchman and Wu 2009b). It can be also used for soils with low friction angles (Herle and Kolymbas 2004) and clays (Masin 2005, Weifner and Kolymbas 2007).

Hypoplastic constitutive models without a characteristic length can describe realistically the onset of shear localization, but not its further evolution. In order to account for the post bifurcation behaviour, a characteristic length can be introduced into the hypoplastic model by means of micro-polar, non-local or second-gradient theories (Tejchman 2004) . In this paper, a micro-polar theory was adopted. The micro-polar model makes use of rotations and couple stresses, which have clear physical meaning for granular materials. In general, the stress and strain tensor is not symmetric. The rotations can be observed during shearing and remain negligible during homogeneous deformation (Oda 1993). Pasternak and Mühlhaus (2001) demonstrated that the additional rotational degree of freedom of a micro-polar continuum arises naturally by mathematical homogenization of an originally discrete system of spherical grains with contact forces and contact moments.

A micro-polar continuum which is a continuous collection of particles behaving like rigid bodies combines two kinds of deformation at two different levels, viz: micro-rotation at the particle level and macro-deformation at the structural level (Schäfer 1962) . For the case of plane strain, each material point has three degrees of freedom, i.e. two translations and one independent rotation (Fig.1). The gradients of the rotation are related to the curvatures, which are associated with the couple stresses. The presence of the couple stresses gives rise to non-symmetry of the stress tensor and to a characteristic length.

A brief summary of the micro-polar hypoplatic constitutive law for plane strain is given in the Appendix (see also Tejchman et al. 2007, Tejchman 2008, Tejchman and Górski 2008, Tejchman and Wu 2009). The constitutive relationship requires the following ten material parameters: e_{i0}, e_{d0}, e_{c0}, ϕ_c, h_s, β, n ,α, a_c and d_{50}. The calibration method for the first eight material parameters can be found in Bauer (1996) and Herle and Gudehus (1999). The parameters h_s and n are estimated from a single oedometric compression test with an initially loose specimen (h_s reflects

the slope of the curve in a semi-logarithmic representation, and n its curvature). The constants α and β are found from a triaxial or plane strain test with a dense specimen and trigger the magnitude and position of the peak friction angle. The angle ϕ_c is determined from the angle of repose or measured in a triaxial test with a loose specimen. The values of e_{i0}, e_{d0}, e_{c0} and d_{50} are obtained with conventional index tests ($e_{c0} \approx e_{max}$, $e_{d0} \approx e_{min}$, $e_{i0} \approx (1.1\text{-}1.5) e_{max}$). In turn, a micro-polar parameter a_c (Eq.20) can be correlated with the grain roughness. This correlation can be established by studying the shearing of a narrow granular strip between two rough boundaries (Tejchman and Gudehus 2001) . It can be represented by a constant, e.g. a_c=1-5, or connected to the parameter a_1^{-1}, e.g. $a_c=(0.5\text{-}1.5)\times a_1^{-1}$. The parameter a_1^{-1} lies in the range of 3.0-4.3 for usual critical friction angles between 25° and 35°. The FE-analyses were carried out with the material constants for the so-called Karlsruhe sand (Bauer 1996, Tejchman and Gudehus 2001): e_{i0}=1.30, e_{d0}=0.51, e_{c0}=0.82, ϕ_c=30°, h_s=190 MPa, β=1, n=0.50, α=0.30, $a_c=a_1^{-1}$ and d_{50}=0.5 mm.

3. FE-input data

The calculations of plane strain compression were performed with the specimen size of $b_o \times h_o$=40×140 mm^2 (b_o – initial width, h_o – initial height). The specimen depth was equal to l=1.0 m with plane strain condition. The width and height of the specimen were similar as in the experiments by Vardoulakis (1980) with the same sand. In all calculations, 896 quadrilateral elements divided into 3584 triangular elements were used. To properly capture shear localization inside of the specimen, the size of the finite elements was smaller than five times of the mean grain diameter d_{50} (Tejchman and Gudehus 2001). The quadrilateral elements composed of four diagonally crossed triangles were used to avoid volumetric locking due to volume changes. Linear shape functions were used for displacements and for the Cosserat rotations. The integration was performed with one sampling point placed in the middle of each triangular element.

Quasi-static deformation in the specimen was imposed through a constant vertical displacement increment Δu prescribed at nodes along the upper edge of the specimen. Two sets of boundary conditions were assumed. First, the top and bottom boundaries were assumed to be ideally smooth, i.e. there is no shear stress along these boundaries. To preserve the stability of the specimen against horizontal sliding, the node in the middle of the top edge was kept fixed. To simulate a movable roller bearing in the experiment (Vardoulakis 1980), the horizontal displacements along the specimen bottom were constrained to move by the same amount from the beginning of

compression. Second, comparative calculations were performed with a very rough top and bottom boundary. In this case, the horizontal displacement and Cosserat rotation along both horizontal boundaries were assumed to be equal to zero. The vertical displacement increments were chosen to be $\Delta u/h_o=2.5\times10^{-6}$. Some 6000 steps were needed to reach a vertical strain of about 25%.

As an initial stress state, a K_0-state with $\sigma_{22}=\gamma_d x_2$ and $\sigma_{11}=K_0\gamma_d x_2$ was assumed in the specimen; σ_{11} - horizontal normal stress, σ_{22} - vertical normal stress; x_2 is the vertical coordinate measured from the top of the specimen, γ_d denotes the unit weight and K_0 is the earth pressure coefficient at rest. The calculations were carried out for three different initial densities, i.e. dense, medium dense and loose. The corresponding parameters are as follows: γ_d=17.0 kN/m^3 and K_0=0.45 for e_o=0.55, γ_d=16.0 kN/m^3 and K_0=0.50 for e_o=0.70, γ_d=14.5 kN/m^3 and K_0=0.55 for e_o=0.90. A uniform confining pressure of σ_c=200 kPa was prescribed.

For the solution of the non-linear equation system, a modified Newton-Raphson scheme with line search was used. The global stiffness matrix was calculated with only the linear terms of the constitutive equations (Eqs.12 and 13). The stiffness matrix was updated every 100 steps. In order to accelerate the convergence in the softening regime, the initial increments of displacements and Cosserat rotations in each calculation step were assumed to be equal to the final increments in the previous step. The procedure was found to yield sufficiently accurate solutions with fast convergence. The magnitude of the maximum out-of-balance force at the end of each calculation step was found to be less than 1-2% of the calculated total vertical force. Due to the non-linear terms in deformation rate and the strain softening, this procedure turned out to be more efficient than the full Newton-Raphson method. The iteration steps were performed using translational and rotational convergence criteria. For the time integration of stress increments in finite elements, a one-step Euler forward scheme was applied. To obtain more accurate results, a sub-stepping algorithm was used; the deformation and curvature increments were further divided into 100 substeps. The calculations were carried out with large deformations and curvatures using a so-called "Updated Lagrangian" formulation by taking into account the Jaumann stress rate, the Jaumann couple stress rate and the actual shape and area of the finite elements. Compressive stress and shortening strain were taken as negative. The calculations were carried out with true strains.

The internal mobilized friction angle was calculated by the following formula

$$\sin\phi = \frac{t}{s}, \tag{1}$$

with the mean stress s and the shear stress t defined by

$$s = 0.5(\sigma_1 + \sigma_3) \qquad \text{and} \qquad t = 0.5(\sigma_1 - \sigma_3), \tag{2}$$

where σ_1 and σ_3 are the principal stresses

$$\sigma_{1,3} = \frac{\sigma_{11} + \sigma_{22}}{2} \pm \sqrt{(\frac{\sigma_{11} - \sigma_{22}}{2})^2 + (\frac{\sigma_{12} + \sigma_{21}}{2})^2}. \tag{3}$$

The mobilized dilatancy angle was defined by

$$\sin\psi = \frac{\dot{\nu}}{\dot{\gamma}}, \tag{4}$$

wherein the volumetric strain rate $\dot{\nu}$ and shear strain rate $\dot{\gamma}$ are

$$\dot{\nu} = d_1 + d_3 \qquad \text{and} \qquad \dot{\gamma} = d_1 - d_3, \tag{5}$$

respectively, with d_1 and d_3 as the principal strain rates. Note that elastic and plastic deformations are not distinguished in hypoplasticity.

$$d_{1,3} = \frac{d_{11} + d_{22}}{2} \pm \sqrt{(\frac{d_{11} - d_{22}}{2})^2 + (\frac{d_{12} + d_{21}}{2})^2}. \tag{6}$$

Non-coaxiality refers to the symmetric part of the stress and the strain rate tensor. Since the stress and strain rate tensor are in general non-symmetric in a micro-polar continuum ($\sigma_{12} \neq \sigma_{21}$ and $d_{12} \neq d_{21}$), non-coaxiality is expressed as the deviation angle between the direction of the principal stress α and the direction of the principal strain rate β as follows

$$\xi = |\alpha - \beta|, \tag{7}$$

using the symmetric part of the stress tensor $0.5(\sigma_{12}+\sigma_{21})$ and the symmetric part of the strain rate tensor $0.5(d_{12}+d_{21})$. The angle α is the orientation of the major principal stress σ_1

$$\tan 2\alpha = \frac{\sigma_{12} + \sigma_{21}}{\sigma_{11} - \sigma_{22}}, \tag{8}$$

and β is the orientation of the major principal rate of deformation d_1

$$\tan 2\beta = \frac{d_{12} + d_{21}}{d_{11} - d_{22}}. \tag{9}$$

Note that the stress and strain rate in the above expressions depend on coordinates and are therefore local variables. As a consequence, the non-coaxiality defined above is local, too.

The relation between the mobilized friction angle and dilatancy angle is known as the stress-dilatancy rule, which is important in studying the mechanical behavior of dilatant granular materials. In this paper comparison is made between the numerical results and the following three stress-dilatancy rules of soil plasticity from the literature.

(1) the stress-dilatancy rule by Gutierrez and Vardoulakis (2007)

$$\sin\psi = (\cos 2\xi) \times \sin\phi \ - \sin\phi_{cx}. \tag{10}$$

(2) the stress-dilatancy rule by Vardoulakis and Georgopoulos (2005) as a modified Taylor's stress-dilatancy rule:

$$\tan\psi = (\cos 2\xi) \times \tan\phi \ - \tan\phi_{cx}. \tag{11}$$

(3) the stress-dilatancy rule by Wan and Guo (2004):

$$\sin\psi = \frac{4}{3}\frac{(\sin\phi - \sin\phi_{cx})}{(1 - \sin\phi\sin\phi_{cx})}. \tag{12}$$

with ϕ as the mobilized friction angle and ϕ_{cx} as the friction angle at the transition from initial contractancy to dilatancy. Eq.10 was derived from the consideration of the dissipation energy of granular material written in terms of the stress and plastic strain rate invariants and by taking into account a difference between the orientation of the major principal stress and the major principal plastic strain rate. Eq.11 is the same as Eq.10 with the function *sin* replaced by the function *tan)*. Eq. 11 was derived from the incremental work done by stresses during a direct shear test. In turn, Eq.12 is an improvement of the classical Rowe's stress dilatancy equation, where an additional factor 4/3 was introduced and the critical friction angle was replaced by the angle ϕ_{cx}.

The stress-dilatancy rules in Eqs.10-12 show the following tendency. Starting from K_o stress state, the dilatancy angle is initially negative, i.e. material undergoes contractancy, then the material experiences significant dilatancy with its maximum at the peak friction angle. Beyond the peak the dilatancy angle decreases and approach gradually zero to reach the critical (residual) state.

The global angle of non-coaxiality ξ can be also calculated from Eq.10 as

$$\cos 2\xi = \frac{\sin\phi_{cx} - \sin\psi}{\sin\phi}. \tag{13}$$

4. Numerical FE-results

Deformed meshes

Figure 2 shows the deformed meshes together with the distribution of void ratio *e* (increase of *e* is indicated by darker shadow). In the case of smooth walls, only one shear zone inside the specimen was observed For very rough boundaries, two shear zones were formed (two intersecting shear zones or two branching shear zones).

The thickness of the shear zone measured at the mid-point of the specimen is about $15\times d_{50}$ (e_o=0.55), $20\times d_{50}$ (e_o=0.70) and $30\times d_{50}$ (e_o=0.90) for smooth and very rough walls (on the basis of shear deformation). Its inclination against the horizontal is about $\theta \approx 52^o$ (e_o=0.55), $\theta \approx 48^o$ (e_o=0.70) and $\theta \approx 46^o$ (e_o=0.90) for smooth walls and $\theta \approx 47^o$ (e_o=0.55), $\theta \approx 46^o$ (e_o=0.70) and $\theta \approx 45^o$ (e_o=0.90) for very rough walls.

The calculated thickness of the shear zone $15\times d_{50}$ (e_o=0.55) for smooth boundaries and initially dense sand is in agreement with the experimental value of $13\times d_{50}$ (Vardoulakis 1980, Vardoulakis and Georgopoulos 2005). In turn, the calculated inclination of the shear zone of 52° against the horizontal is slightly smaller as compared to the inclination of 57° in experiment (Vardoulakis and Georgopoulos 2005).

Internal friction angle

Fig.3A and Fig.4 show the evolution of the mobilized friction angle ϕ calculated with global and local principal stresses (Eq.1). The global principal stresses were calculated according to $\sigma_1=P/bl$ (P – resultant vertical force, b – actual specimen width) and $\sigma_3=\sigma_c$. The local stresses were calculated by Eq.3 at the different mid-points of shear zones (at $x_1=b_o/4$, $b_o/2$ and $3b_o/4$, respectively).

For smooth walls, the mobilized global friction angle increases to reach a pronounced peak and drops gradually at large deformation (the residual state has not been reached at u_2^t/h_o=25%). The global peak friction angles are: ϕ_p=51.5° at u_2^t/h_o=0.022 (e_o=0.55), ϕ_p=37.7° at u_2^t/h_o=0.029 (e_o=0.70) and ϕ_p=30.3° at u_2^t/h_o=0.08 (e_o=0.90), respectively. For comparison, the global friction angles at large deformation of u_2^t/h_o=25% are about: ϕ_{res}=29.0° (e_o=0.55), ϕ_{res}=27.0° (e_o=0.70) and ϕ_{res}=23.0° (e_o=0.90), respectively.

As compared to very smooth boundaries, the evolution of the mobilized global friction angle is different with very rough boundaries. Along with deformation, the global friction angle increases to a pronounced peak, drops gradually to reach a residual state. The global peak friction angles are: ϕ_p=51.7° at u_2^t/h_o=0.021 (e_o=0.55), ϕ_p=38.2° at u_2^t/h_o=0.029 (e_o=0.70) and ϕ_p=30.9° at u_2^t/h_o=0.06 (e_o=0.90), respectively. The global residual friction angles at large deformation of u_2^t/h_o=25% are about: ϕ_{res}=43° (e_o=0.55), ϕ_{res}=38° (e_o=0.70) and ϕ_{res}=30° (e_o=0.90), respectively. Thus, the peak friction angles are only slightly higher (by 0.2°-0.7°) and the friction angles at large deformation of u_2^t/h_o=25% are significantly higher (by 7°-14°) than for smooth walls.

Usually, the local friction angles in shear zones reach their asymptotic values (except of points where two shear zones intersect each other, i.e. in the cases with very rough boundaries and e_o=0.55 and e_o=0.70). The local peak friction angles are similar as the global values

independently of the wall roughness. For smooth walls, the mean local residual friction angles are significantly higher than the global ones (by 5^o-7^o). In the case of very rough walls, the mean local residual friction angles are significantly lower than the global ones for e_o=0.55 and e_o=0.70 (by 4^o-12^o) or higher for e_o=0.90 (by 4^o).

The evolution of the calculated global internal friction angle with smooth walls (e_o=0.55 and e_o=0.70) is similar as in the experiment (Vardoulakis 1980) although the calculated residual friction angle is somewhat lower by about 4^o.

Contractancy/dilatancy angle

The evolution of the mobilized global and local (in the mid-point of the shear zone) dilatancy/contractancy angle ψ is demonstrated in Figs.3B and 5. The dilatancy/contractancy angle was calculated according to Eqs.4 and 5. All global dilatancy/contractancy curves are seen to be smooth. They show (independently of e_o) initial contractancy (up to u_2^t/h_o=0.025-0.10) followed by dilatancy for initially dense and medium dense sand or further contractancy for initially loose sand. The peak dilatancy angles are about: 22^o-24° for e_o=0.55 and 5° for e_o=0.70. At large deformation for smooth boundaries, the dilatancy angle for initially dense sand (e_o=0.55) decreases gradually to approach the zero value in the residual state. In the case of e_o=0.70, the dilatancy also decreases gradually reaching again the region contractancy. When the specimen is initially loose (e_o=0.90), contractancy slightly continuously increases.

In the case of very rough walls, the dilatancy angle for e_o=0.55 and e_o=0.70 decreases gradually and increases next again with increasing deformation. When the specimen is initially loose, contractancy continuously decreases reaching the asymptote at $+5^o$.

Usually, the local dilatancy angles in the shear zones reach their asymptotic values except the cases with very rough boundaries (initially dense and medium dense sand). The local peak dilatancy angles are similar as the global values independently of the wall roughness. For smooth walls, the mean local residual dilatancy angles are higher than the global ones at large deformation u_2^t/h_o=0.25 (by 10^o-35^o). In the case of very rough walls, the mean local residual dilatancy angles can be in some points of shear zones significantly higher than the global ones (by 5^o-35^o). An abrupt change of contractancy to dilatancy during shear zone occurrence close to the peak (observed in experiments with initially dense sand by Vardoulakis 1980) was only observed with initially loose sand. In contrast to global dilatancy curves, the local dilatancy

curves indicate pronounced oscillations in the shear zone for 3 cases: in initially loose sand with smooth boundaries at peak (u_2^t/h_o=0.03-0.08) and in some points of initially dense and medium dense sand with very rough boundaries for large vertical deformation (u_2^t/h_o=0.15-0.25). Oscillations of volume changes at the residual state were observed in experiments by Vardoulakis (1980) with initially dense specimens. Approximately, the evolution of local dilatancy/contractancy is similar to the evolution of local friction.

The shape of the calculated global dilatancy curves (smooth boundaries, e_o=0.55 and e_o=0.70) is similar as in the experiment (Vardoulakis and Georgopoulos 2005, Vardoulakis 1980). The calculated peak and residual values show similar trend.

Non-coaxiality

Finally, the evolutions of the local angle of non-coaxiality ξ (Eq.7) in the mid-point of the shear zone at $x_1=b_o/4$, $x_1=b_o/2$ and $x_1=3b_o/4$ for different initial void ratios are depicted in Fig.6 (smooth and very rough walls). As can be seen from Fig.6, the deviation angle between the principal stress and the principal strain-rate directions is insignificant with $\xi\approx$1-4^o at the peak (smooth boundaries) independently of e_o, except of the case with initially loose sand where strong oscillations occur ($\xi=\pm25^0$). At smooth boundaries with large vertical deformation of u_2^t/h_o=0.25, the deviation angle ξ in the mid-point of the shear zone increases with increasing e_o and is only about 2^o (e_o=0.55-0.90).

In the case of very rough boundaries, at large vertical deformation of u_2^t/h_o=0.25, the deviation angle ξ in some mid-points of the shear zones increases significantly with decreasing e_o and can be about 1^o (e_o=0.90), 30^o (e_o=0.70 and e_o=0.55). It is to note that large deviations angles ξ appear only in some points of the shear zones (point '*b'* at e_o=0.70, and points '*b*' and '*e*' at e_o=0.70). This angle can significantly oscillate with initially dense and medium dense sand.

The local oscillations of non-coaxiality are connected to the local oscillations of dilatancy angle. They merit further investigations.

The global angle of non-coaxiality ξ can be calculated with Eq.7 or Eq.12. For initially dense and medium dense sand the friction angles are: ϕ_{cx}=40^o and ϕ_{cx}=36^o, respectively (independently of e_o). The mobilized global angles are: ψ=20^o and ϕ=52^o (e_o=0.55), and ψ=5^o and ϕ=38^o

(e_o=0.70) at peak and ψ=-10°-0° and ϕ=28°-30° (smooth walls), ψ=15°-20° and ϕ=38°-43° (very rough walls) at large deformation (Fig.3A and Fig.3B), respectively. The global deviation angles ξ are ξ=20°-30° (peak and large deformation) and are far from the calculated ones in the shear zones. Since $\sin\phi_{cx} - \sin\psi > \sin\phi$ in Eq.12, the dilatancy angle cannot be determined for some cases (e.g. very rough walls with e_o=0.55 and e_o=0.70).

The values of calculated mean local dilatancy angles at peak for initially dense and medium dense sand (smooth and very rough walls) were compared with those given by Eq.10-12. It can be seen from Tab.1 that Eqs.11 and 12 provide the most realistic results at peak.

As compared to experiments (smooth walls, initially dense and medium dense sand), the calculated angle ξ shows similar behaviour as the global one on the same sand (Vardolulakis and Geporgopoulos 2005). Our numerical results collaborate well also with the experimental finding by Arthur and Assadi (1977), where similar non-coaxiality of 6-12° was observed in the shear zone. However, this calculated effect of non-coaxiality is found to be much smaller at the residual state than e.g. in the experiments on Nevada sand (ξ=30°) (Gutierrez and Vardoulakis 2007), which is in turn similar as the numerical results with very rough walls.

Moreover, the calculated evolution of the deviation angle between the principal stress and the principal strain rate directions (smooth boundaries, dense sand) is similar as reported by Tordesillas (2009) using a micromechanical model (about 6° at peak and 0° at residual state). However, it is significantly smaller at the peak than the numerical result from discrete element simulations, i.e. 40°, but similar at the residual state (about $\xi \cong 0$) (Thornton and Zhang 2006).

5. Conclusions

Our numerical results suggest that the boundary conditions have considerable effect beyond the peak, where a shear zone is fully developed. This can be ascertained with respect to mobilized friction, dilatancy and non-coaxiality (i.e. the global quantities can significantly differ from the local ones in the shear zones). The pattern of shear zones seems to depend on the boundary conditions, too, in particular on the roughness of top and bottom-plates. The numerical calculations with smooth plates show one single shear zone, whereas rough plates give rise to two intersecting shear zones. The thickness of the shear zone is found to increase with increasing

initial void ratio and remains fairly independent of the wall roughness. The shear zone inclination increases with decreasing void ratio and decreasing wall roughness.

Both the global and local internal friction angles at the peak increase with decreasing void ratio and remain fairly independent of the boundary roughness. However, the residual friction angle, both global and local, is found to depend on both void ratio and boundary roughness. Similar observations can also be made on the dilatancy angles.

Non-coaxiality is found to be very small prior to the peak and remains moderate (less than 5°) up to fairly large deformation of about 25%. For large deformation, non-coaxiality seems to increase with increasing boundary roughness. Pronounced local non-coaxiality of about 30^o can be observed inside the shear band for initially dense sand. Inside the shear zones, the stress-dilatancy rules in the literature (Eqs.10-12) can be confirmed up to the peak. It seems that no of the existing stress-dilatancy rules remain valid in shear zones for large deformation, in particularly in points where shear zones intersect.

Appendix

The constitutive relationship between the rate of stress, the rate of couple stress, the strain rate and the curvature rate can be generally expressed by the following two equations (Tejchman and Górski 2008, Tejchman 2008):

$$\overset{o}{\sigma}_{ij} = F_{ij}(e,\sigma_{kl},m_i,d_{kl}^{\,c},k_i,d_{50}), \tag{14}$$

$$\overset{o}{m}_i = G_i(e,\sigma_{kl},m_i,d_{kl}^{\,c},k_i,d_{50}). \tag{15}$$

The Jaumann stress rate and Jaumann couple stress rate therein are defined by

$$\overset{o}{\sigma}_{ij} = \dot{\sigma}_{ij} - w_{ik}\,\sigma_{kj} + \sigma_{ik}w_{kj} \tag{16}$$

and

$$\overset{o}{m}_i = \dot{m}_i - 0.5w_{ik}m_k + 0.5m_k w_{ki}. \tag{17}$$

The functions F_{ij} and G_i in Eqs.14 and 15 represent isotropic tensor-valued functions of their arguments; σ_{ij} is the Cauchy stress tensor, m_i is the couple stress vector, e denotes the current void ratio, d_{kl}^c is the polar strain rate and k_i denotes the rate of curvature vector:

$$d_{ij}^c = d_{ij} + w_{ij} - w_{ij}^c, \qquad \text{and} \qquad k_i = w_{,i}^c. \tag{18}$$

The strain rate tensor d_{ij} and the spin tensor w_{ij} are related to the velocity v_i as follows:

$$d_{ij} = (v_{i,j} + v_{j,i})/2, \qquad w_{ij} = (v_{i,j} - v_{j,i})/2, \qquad ()_{,i} = \partial()/\partial x_i. \tag{19}$$

The rate of Cosserat rotation w^c is defined by

$$w_{21}^c = -w_{12}^c = w^c \qquad \text{and} \qquad w_{kk}^c = 0. \tag{20}$$

For moderate pressures, the grains can be assumed to be isochoric. In this case, the change of void ratio depends only on the strain rate via

$$\dot{e} = (1+e) d_{kk}. \tag{21}$$

For the numerical calculations, the following micro-polar hypoplastic constitutive equation are employed:

$$\overset{o}{\sigma}_{ij} = f_s [\, L_{ij}(\hat{\sigma}_{kl}, \hat{m}_k, d_{kl}^c, k_k d_{50}) + f_d N_{ij}(\hat{\sigma}_{ij}) \sqrt{d_{kl}^c d_{kl}^c + k_k k_k d_{50}^2}\,] \tag{22}$$

and

$$\overset{o}{m}_i / d_{50} = f_s [\, L_i^c(\hat{\sigma}_{kl}, \hat{m}_k, d_{kl}^c, k_k d_{50}) + f_d N_i^c(\hat{m}_i) \sqrt{d_{kl}^c d_{kl}^c + k_k k_k d_{50}^2}\,], \tag{23}$$

wherein the normalized stress tensor $\hat{\sigma}_{ij}$ is defined by

$$\hat{\sigma}_{ij} = \frac{\sigma_{ij}}{\sigma_{kk}} \tag{24}$$

and the normalized couple stress vector $\hat{m}_i$ is defined by

$$\hat{m}_i = \frac{m_i}{\sigma_{kk} d_{50}}, \tag{25}$$

wherein d_{50} is the mean grain diameter. The scalar factors $f_s = f_s\ (e,\ \sigma_{kk})$ and $f_d = f_d\ (e,\ \sigma_{kk})$ in Eqs.22 and 23 describe the influence of density and stress level on the incremental stiffness. The factor f_s depends on the granulate hardness h_s, the mean stress σ_{kk}, the maximum void ratio e_i and the current void ratio e by:

$$f_s = \frac{h_s}{n h_i} \left(\frac{1+e_i}{e_i}\right) \left(\frac{e_i}{e}\right)^{\beta} \left(-\frac{\sigma_{kk}}{h_s}\right)^{1-n} \tag{26}$$

with

$$h_i = \frac{1}{c_1^2} + \frac{1}{3} - \left(\frac{e_{i0} - e_{d0}}{e_{c0} - e_{d0}}\right)^{\alpha} \frac{1}{c_1 \sqrt{3}}. \tag{27}$$

In the above equations, the granulate hardness h_s represents a reference pressure, the coefficients α and β express the dependence on density and pressure respectively, and n denotes the compression coefficient. The multiplier f_d represents the dependence on a relative void ratio via:

$$f_d = \left(\frac{e - e_d}{e_c - e_d}\right)^{\alpha}. \tag{28}$$

The relative void ratio in the above expression involves the void ratio in critical state e_c, the minimum void ratio e_d (the densest packing) and the maximum void ratio e_i (the loosest packing). In a critical state, a granular material experiences continuous deformation while the void ratio remains unchanged. The current void ratio e is bounded by the two extreme void ratios e_i and e_d. Based on experimental observations, the void ratios e_i, e_d and e_c are assumed to depend on the pressure σ_{kk}:

$$e_i = e_{i0} \exp\left[-\left(-\sigma_{kk} / h_s\right)^n\right], \tag{29}$$

$$e_d = e_{d0} \exp\left[-\left(-\sigma_{kk} / h_s\right)^n\right], \tag{30}$$

$$e_c = e_{c0} \exp\left[-\left(-\sigma_{kk} / h_s\right)^n\right], \tag{31}$$

wherein e_{i0}, e_{d0} and e_{c0} are the values of e_i, e_d and e_c at $\sigma_{kk}=0$, respectively. For the functions L_{ij}, N_{ij}, L_i^c and N_i^c, the following specific expressions are used:

$$L_{ij} = a_1^2 d_{ij}^c + \hat{\sigma}_{ij}(\hat{\sigma}_{kl}\, d_{kl}^c + \hat{m}_k\, k_k d_{50}), \tag{32}$$

$$L_i^c = a_1^2 k_i d_{50} + a_1^2\, \hat{m}_i(\hat{\sigma}_{kl}\, d_{kl}^c + \hat{m}_k\, k_k d_{50}), \tag{33}$$

$$N_{ij} = a_1(\hat{\sigma}_{ij} + \hat{\sigma}_{ij}^*), \tag{34}$$

$$N_i^c = a_1^2 a_c\, \hat{m}_i, \tag{35}$$

where

$$a_1^{-1} = c_1 + c_2\sqrt{\hat{\sigma}_{kl}^*\, \hat{\sigma}_{lk}^*}\,[1 + cos(3\theta)], \tag{36}$$

$$cos(3\theta) = -\frac{\sqrt{6}}{[\hat{\sigma}_{pq}^*\, \hat{\sigma}_{pq}^*]^{1.5}}(\hat{\sigma}_{kl}^*\, \hat{\sigma}_{lm}^*\, \hat{\sigma}_{mk}^*) \tag{37}$$

with

$$c_1 = \sqrt{\frac{3}{8}}\frac{(3 - sin\phi_c)}{sin\phi_c}, \qquad c_2 = \frac{3}{8}\frac{(3 + sin\phi_c)}{sin\phi_c}. \tag{38}$$

The parameter a_1 is the deviatoric part of the normalized stress in critical states (Bauer 1996), ϕ_c is the friction angle in critical states, and the parameter θ denotes the Lode angle in the deviatoric plane at $\hat{\sigma}_{ii}$ =1, and $\hat{\sigma}_{ij}^*$ denotes the deviatoric part of $\hat{\sigma}_{ij}$.

References

Arthur, J. R. F. and Assadi, A. (1977). Ruptured sand sheared in plane strain. *Proc. 9th Int. Conf. Soil Mech. Foundation Engineering,* Tokyo 1, 19-22.

Bauer, E. (1996). Calibration of a comprehensive hypoplastic model for granular materials. *Soils and Foundations* 36(1): 13-26.

Desrues, J., Chambon, R., Mokni, M. and Mazerolle, F. (1996). Void ratio evolution inside shear bands in triaxial sand specimens studied by computed tomography. *Géotechnique* 46(3):529-546.

Gudehus, G. (1996). A comprehensive constitutive equation for granular materials. *Soils and Foundations* 36(1): 1-12.

Gudehus, G. (2006). Seismo-hypoplasticity with a granular temperature. *Granular Matter,* 8, 93-102.

Gutierrez, M. and Vardoulakis, I. (2007). Energy dissipation and post-bifurcation behaviour of granular soils. *Int. J. Num. and Anal. Methods in Geomechanics* 31, pp. 435-455.

Herle, I. and Gudehus, G. (1999). Determination of parameters of a hypoplastic constitutive model from properties of grain assemblies. *Mechanics of Cohesive-Frictional Materials*, 4, 5, 461-486.

Herle, I. and Kolymbas, D. (2004). Hypoplasticity for soils with low friction angles. *Computers and Geotechnics,* 31, 365-373.

Masin, D. (2005). A hypoplastic constitutive model for clays. *Int. J. Numer. and Anal. Meths. in Geomech.*, 29, 311-336.

Masin, D. and Herle, I. (2007). Improvement of a hypoplastic model to predict clay behaviour under undrained conditions, *Acta Geotechnica*, 2, 261-268.

Niemunis, A. and Herle, I. (1997). Hypoplastic model for cohesionless soils with elastic strain range. *Mechanics of Cohesive-Frictional Materials,* 2, 279-299.

Niemunis, A. (2003). Extended hypoplastic models for soils. *Habilitation Monography*, Gdansk University of Technology.

Oda, M. (1993). Micro-fabric and couple stress in shear bands of granular materials. In: *Powders and Grains* (C. Thornton, editor), Rotterdam, Balkema, 161-167.

Pasternak, E. and Mühlhaus, H.-B. (2001). Cosserat continuum modelling of granulate materials. In: *Computational Mechanics – New Frontiers for New Millennium* (eds.: S. Valliappan S. and N. Khalili), Elsevier Science, 1189-1194.

Rondón, HA, Wichtmann, T, Triantafyllidis, T. and Lizcano, A (2007) Hypoplastic material constants for a well-graded granular material for base and subbase layers of flexible pavements, *Acta Geotechnica*, 2: 113-126

Schäfer, H. (1962). Versuch einer Elastizitätstheorie des zweidimensionalen ebenen Cosserat-Kontinuums. Miszellaneen der Angewandten Mechanik, Festschrift Tolmien, W., Berlin, Akademie-Verlag.

Tejchman, J. and Gudehus, G. (2001). Shearing of a narrow granular strip with polar quantities. *I. J. Num. and Anal. Methods in Geomechanics* 25: 1-28.

Tejchman, J. (2004). Influence of a characteristic length on shear zone formation in hypoplasticity with different enhancements. *Computers and Geotechnics* 31, 8, 595-611.

Tejchman, J, Bauer E and Tantono, S. F. (2007) Influence of initial density of cohesionless soil on evolution of passive earth pressure, *Acta Geotechnica*, 2: 53-63.

Tejchman, J., Bauer, E. and Wu, W. (2007). Effect of texturial anisotropy on shear localization in sand during plane strain compression. *Acta Mechanica*, 1-4, 23-51.

Tejchman, J. and Górski, J. (2008). Computations of size effects in granular bodies within micro-polar hypoplasticity during plane strain compression. *Int. J. for Solids and Structures*, 45, 6, 1546-1569.

Tejchman, J. (2008). *FE modeling of shear localization in granular bodies with micro-polar hypoplasticity*. Springer Series in Geomechanics and Geoengineering (eds. Wu and Borja).

Tejchman, J. and Wu, W. (2009a). FE-investigations of non-coaxiality and stress-dilatancy rule in dilatant granular bodies within micro-polar hypoplasticity. *Int. Journal for Numerical and Analytical Methods in Geomechanics*, 33, 1, 117-142.

Tejchman, J. and Wu, W. (2009b). FE-investigations of shear localization in granular bodies under high shear rate, *Granular Matter*, 11, 2, 115-128.

Thornton, C and Zhang, L. (2006). A numerical examination of shear banding and simple shear non-coaxial flow rules. *Philosophical Magazine*. 86. 21-22, 3425-3452.

Tordesillas, A. (2009). Non-coaxiality and force chain evolution. *International Journal of Engineering Science*, (in press).

Wan, R. G. and Guo, P. J. (2004). Stress dilatancy and fabric dependencies on sand behavior. *J. Engng. Mechanics ASCE*, 130, 6, 635-645.

Wang, C. C. (1970). A new representation theorem for isotropic functions. *J. Rat. Mech. Anal*., 36, 166-223.

Weifner, T. and Kolymbas, D. (2007). A hypoplastic model for clay and sand, *Acta Geotechnica*, 2, 103-112.

von Wolffersdorff, P A. (1996). A hypoplastic relation for granular materials with a predefined limit state surface. *Mechanics Cohesive-Frictional Materials* 1: 251-271.

Vardoulakis, I. (1980). Shear band inclination and shear modulus in biaxial tests. *Int. J. Num. Anal. Meth. Geomech.* 4:103-119.

Vardoulakis, I. and Georgopoulos, I. O. (2005). The stress-dilatancy hypothesis revisited: shear-banding related instabilities. *Soils and Foundations* 45, 2, 61-76.

Yoshida, T., Tatsuoka, F. and Siddiquee, MS. (1994). Shear banding in sands observed in plane strain compression. In: R. Chambon, J. Desrues and I. Vardoulakis, editors. *Localisation and Bifurcation Theory for Soils and Rocks.* Balkema, Rotterdam, pp.165-181.

LIST OF FIGURES

Fig.1: Plane strain static Cosserat continuum: a) degrees of freedom (u_1 - horizontal displacement, u_2 -vertical displacement, ω^c - Cosserat rotation), b) stresses σ_{ij} and couple stresses m_i at an element

Fig.2: Deformed FE-meshes with the distribution of void ratio e at residual state: a) smooth boundaries, e_o=0.55, u_2^t/h_o=0.071, b) smooth boundaries, e_o=0.70, u_2^t/h_o=0.071, c) smooth boundaries, e_o=0.90, u_2^t/h_o=0.014, d) very rough boundaries, e_o=0.55, u_2^t/h_o=0.071, e) very rough boundaries, e_o=0.70, u_2^t/h_o=0.071, f) very rough boundaries, e_o=0.90, u_2^t/h_o=0.014

Fig.3: Evolution of mobilized global friction angle ϕ versus normalized vertical displacement of the upper edge u_2^t/h_o, B) evolution of mobilized global dilatancy angle ψ versus normalized vertical displacement of the upper edge u_2^t/h_o: a) smooth boundaries, e_o=0.55, b) smooth boundaries, e_o=0.70, c) smooth boundaries, e_o=0.90, d) very rough boundaries, e_o=0.55, e) very rough boundaries, e_o=0.70, f) very rough boundaries, e_o=0.90

Fig.4: Evolution of mobilized local friction angle ϕ in the mid-points of shear zones versus normalized vertical displacement of the upper edge u_2^t/h_o: a) smooth boundaries, e_o=0.55, b) smooth boundaries, e_o=0.70, c) smooth boundaries, e_o=0.90, d) very rough boundaries, e_o=0.55, e) very rough boundaries, e_o=0.70, f) very rough boundaries, e_o=0.90

Fig.5: Evolution of mobilized dilatancy angle ψ in the mid-points of shear zones versus normalized vertical displacement of the upper edge u_2^t/h_o: a) smooth boundaries, e_o=0.55, b) smooth boundaries, e_o=0.70, c) smooth boundaries, e_o=0.90, d) very rough boundaries, e_o=0.55, e) very rough boundaries, e_o=0.70, f) very rough boundaries, e_o=0.90

Fig.6: Evolution of local non-coaxiality angles $\xi=\alpha-\beta$ versus normalized vertical displacement of the upper edge u_2^t/h_o: a) smooth boundaries, e_o=0.55, b) smooth boundaries, e_o=0.70, c) smooth boundaries, e_o=0.90, d) very rough boundaries, e_o=0.55, e) very rough boundaries, e_o=0.70, f) very rough boundaries, e_o=0.90

LIST OF TABLES

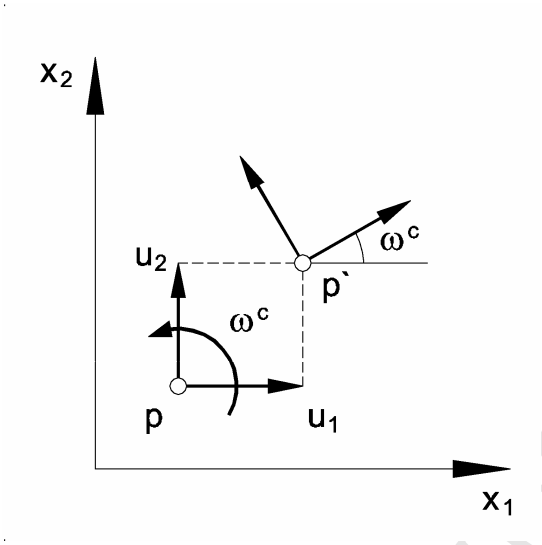

a)

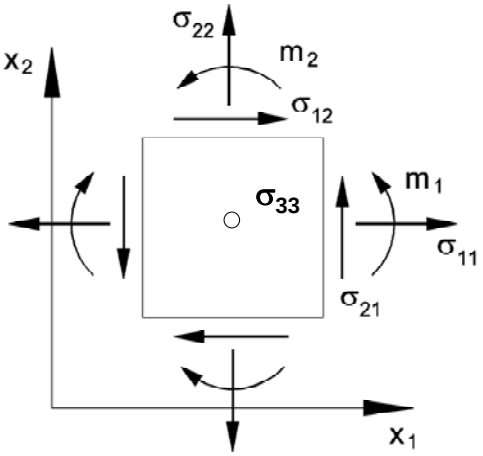

b)

FIGURE 1

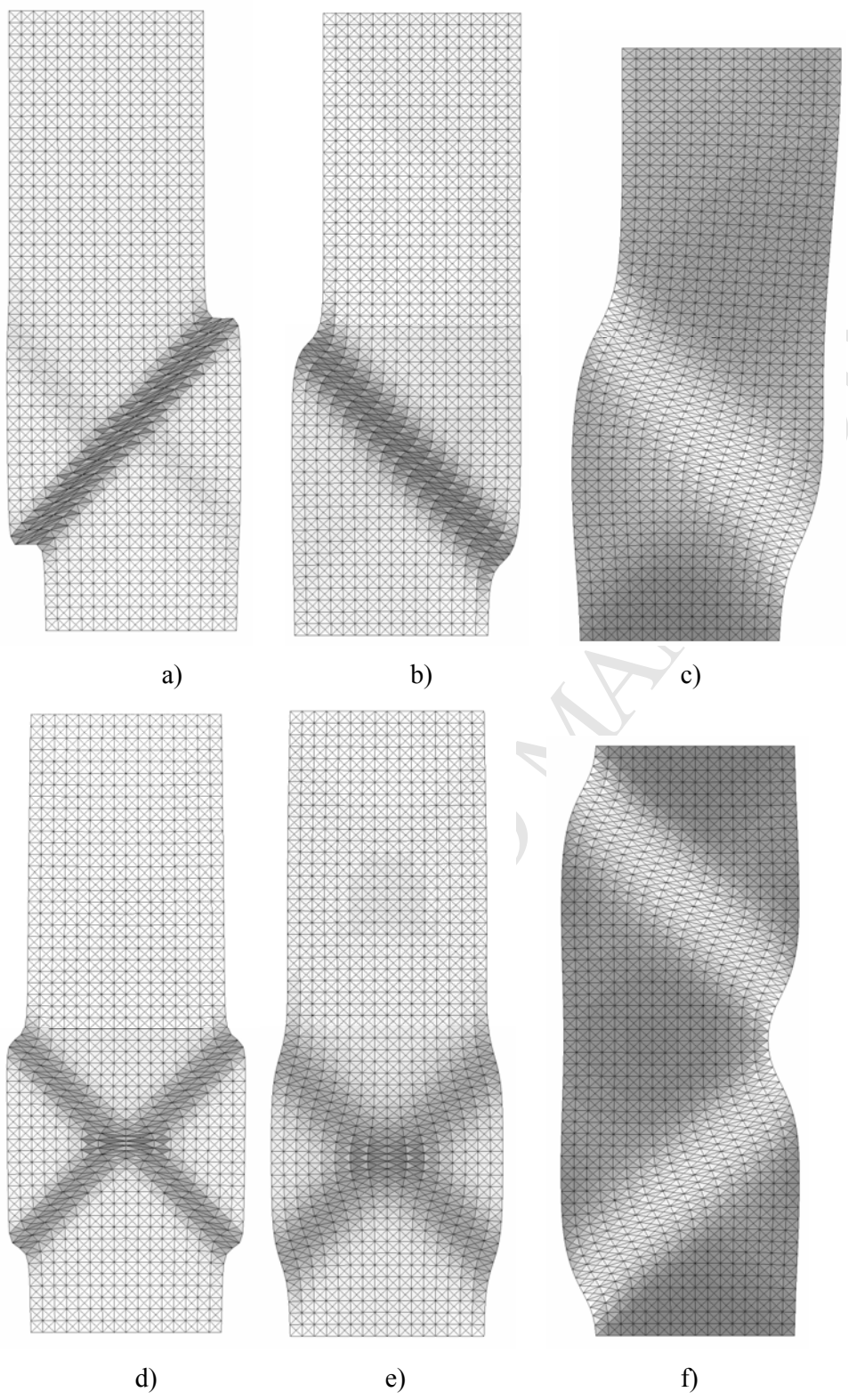

FIGURE 2

A)

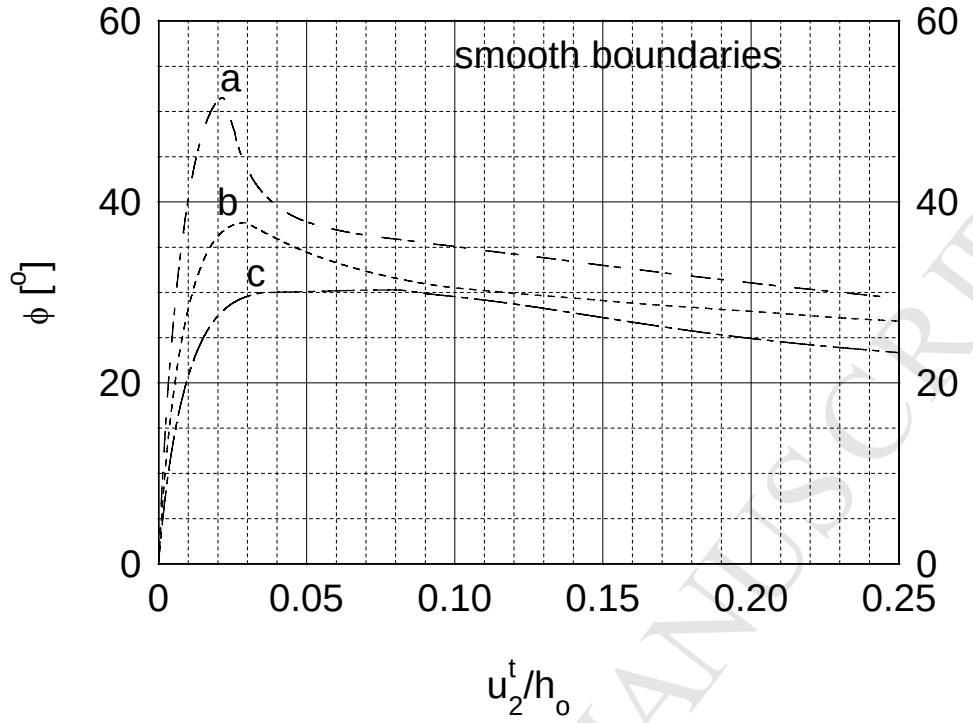

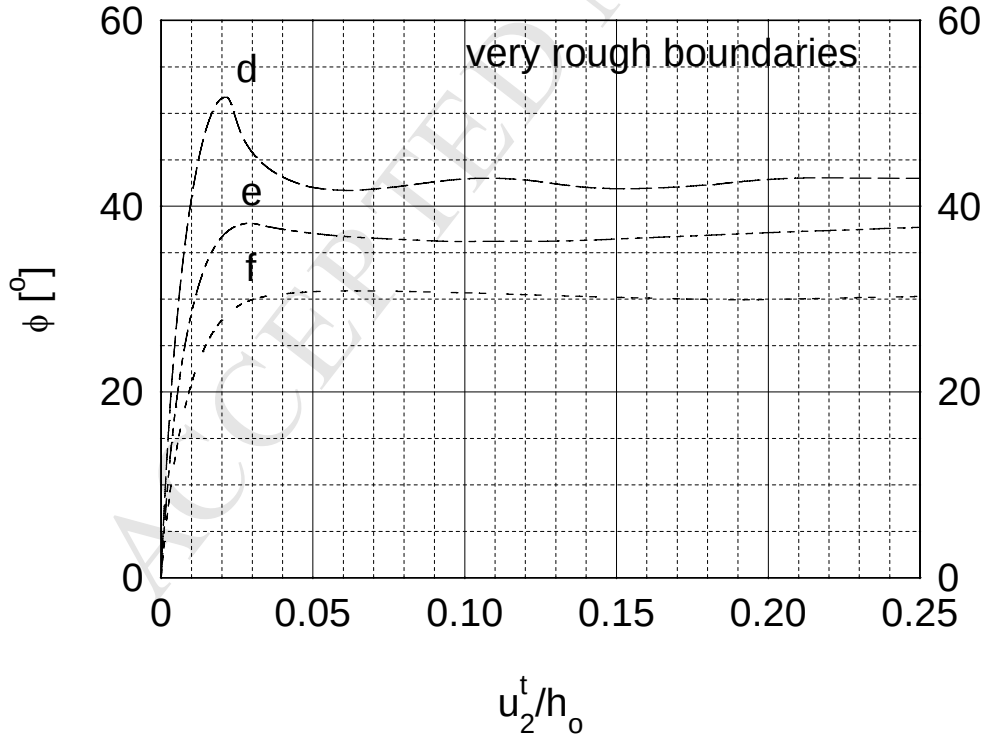

B)

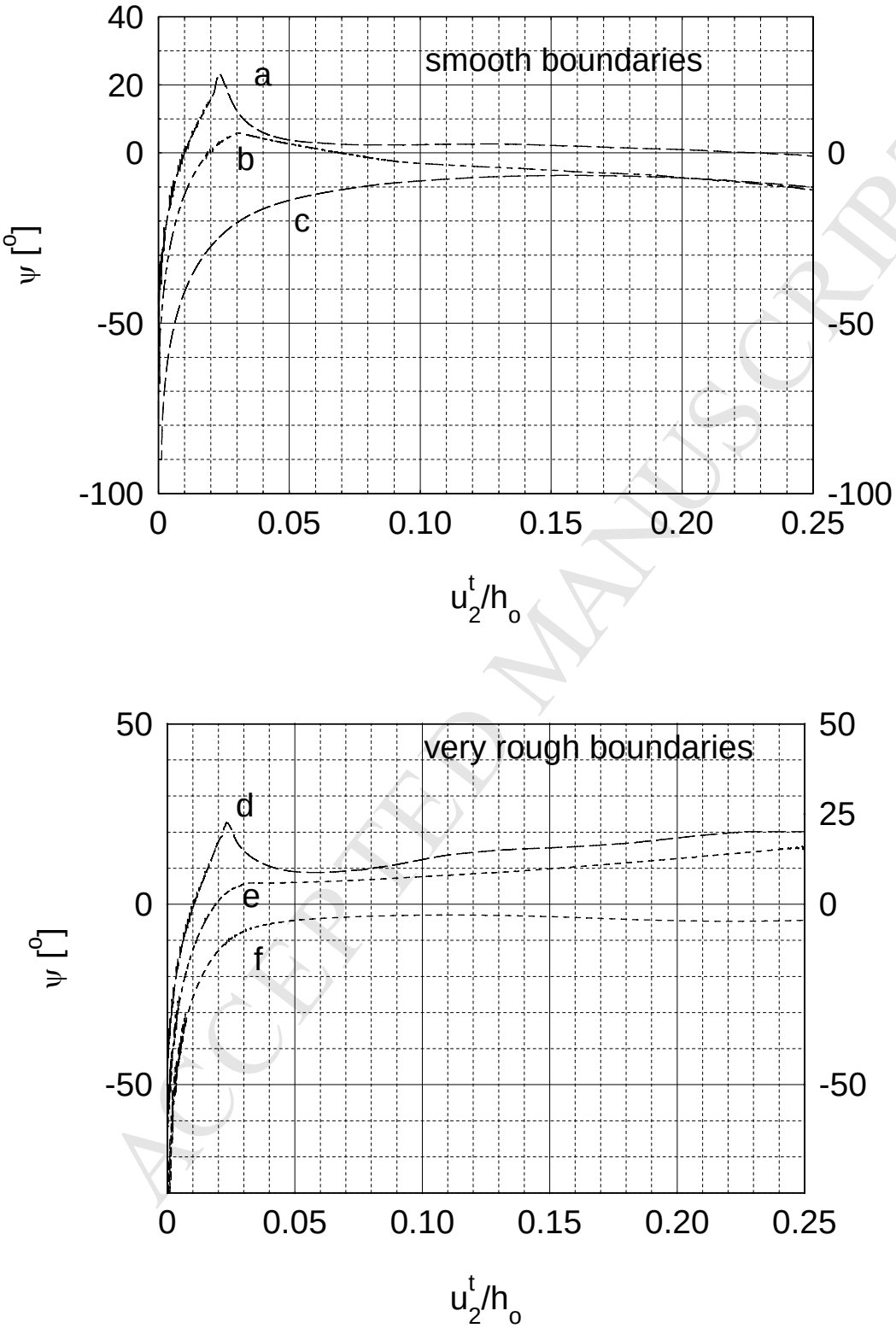

FIGURE 3

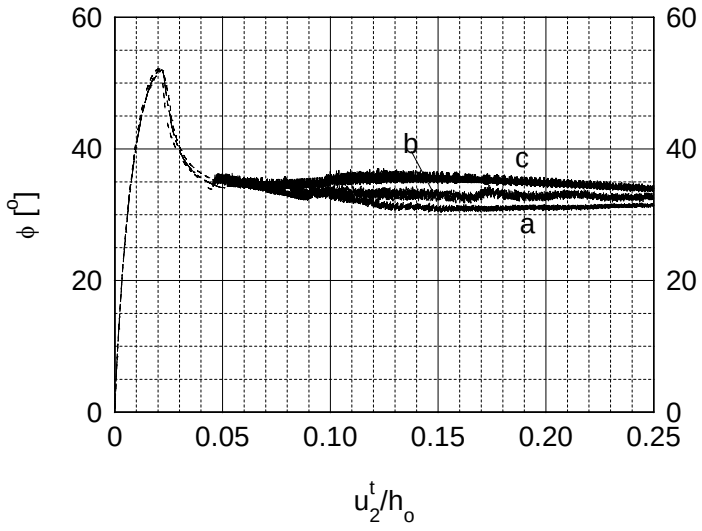

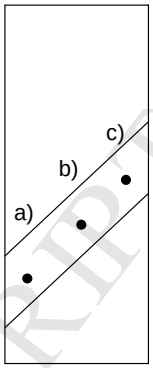

a)

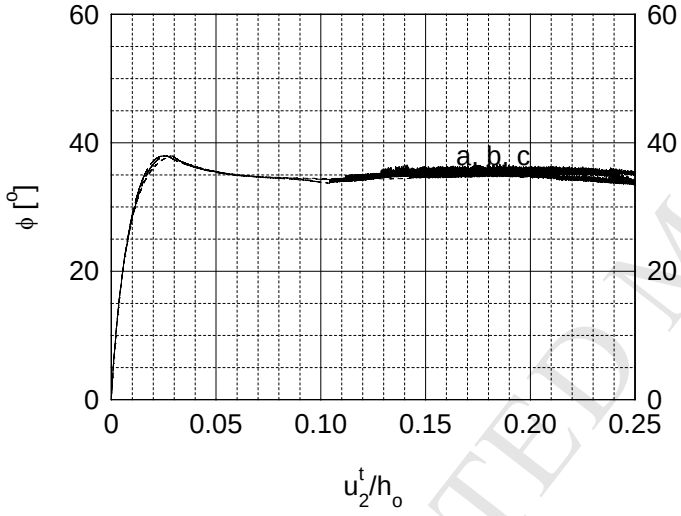

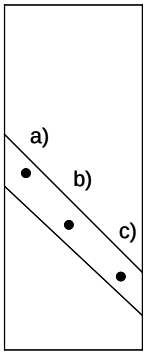

b)

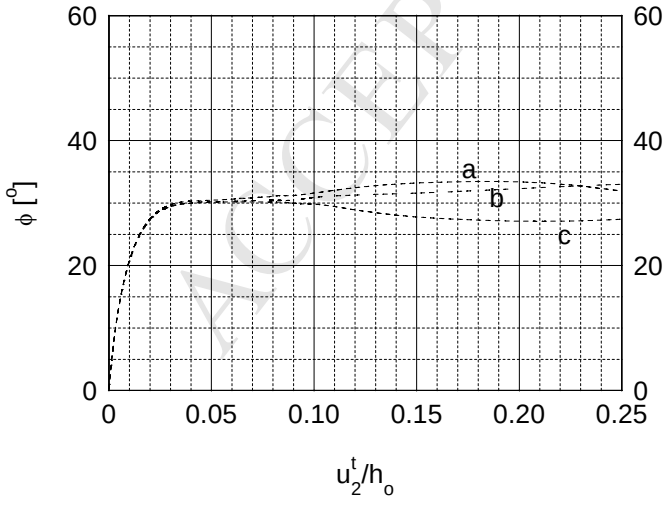

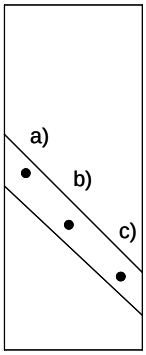

c)

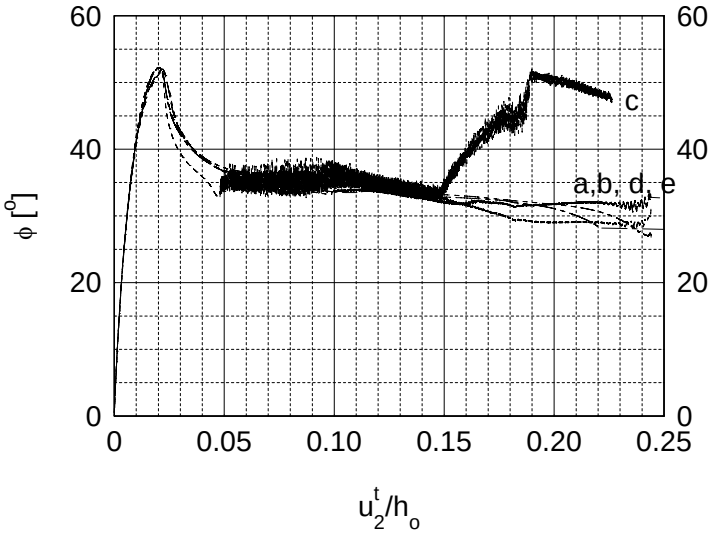

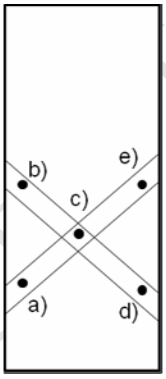

d)

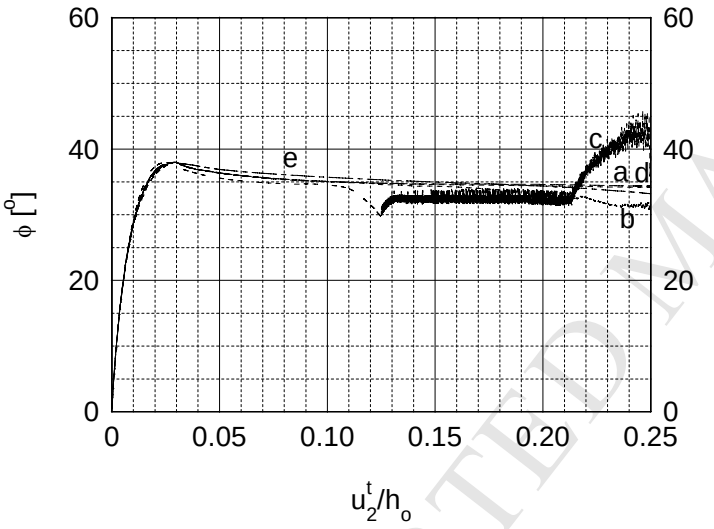

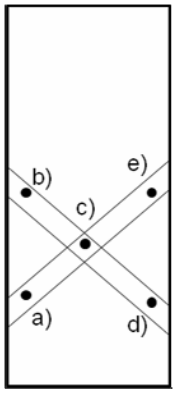

e)

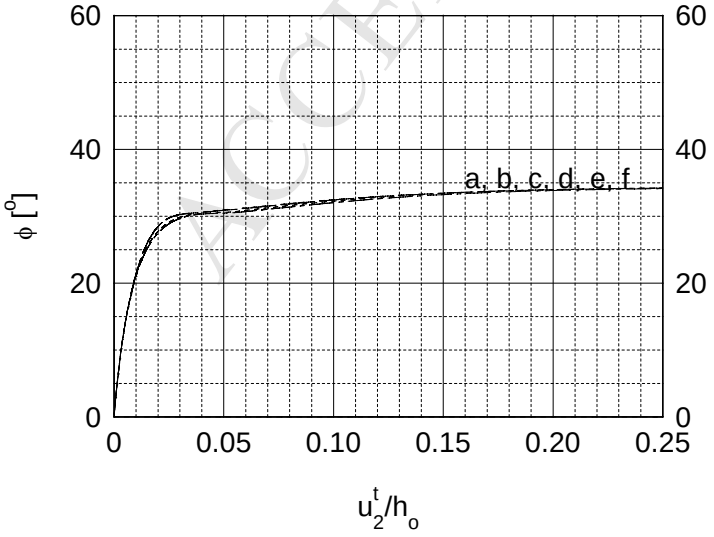

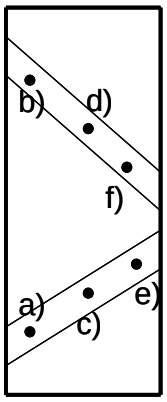

f)

FIGURE 4

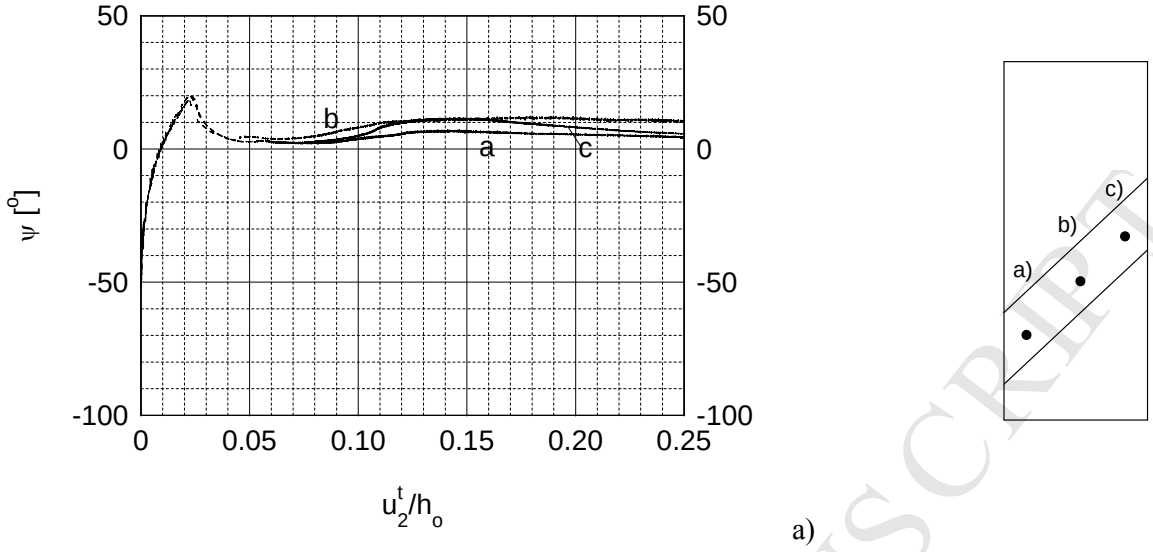

a)

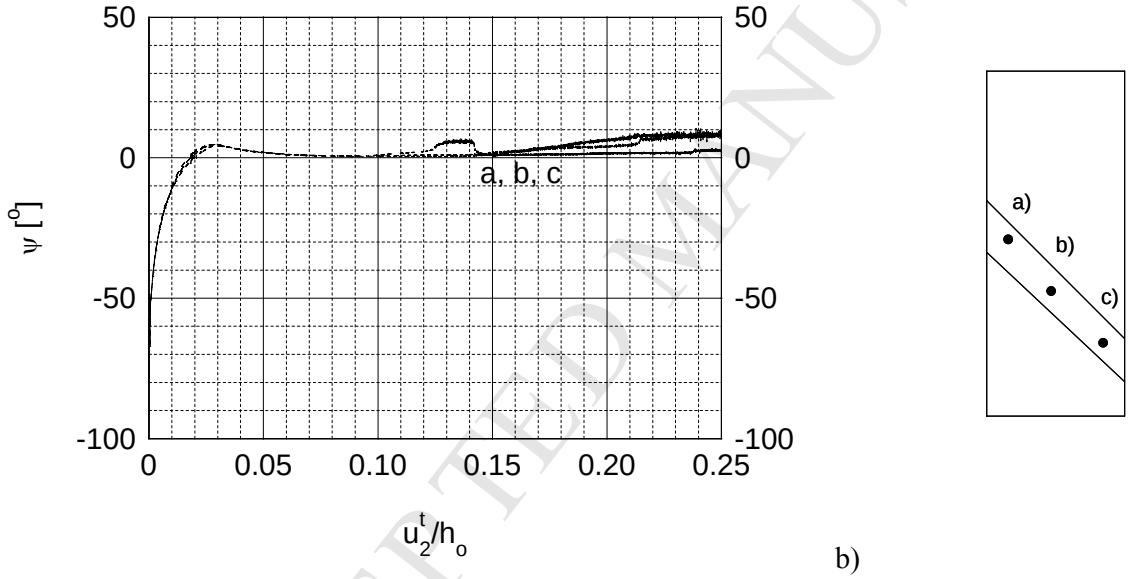

b)

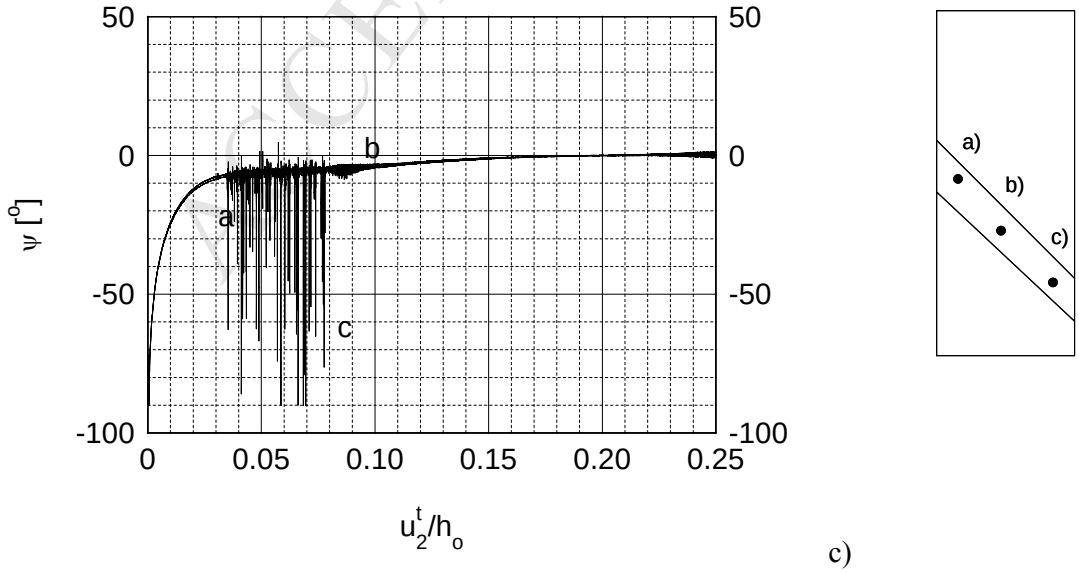

c)

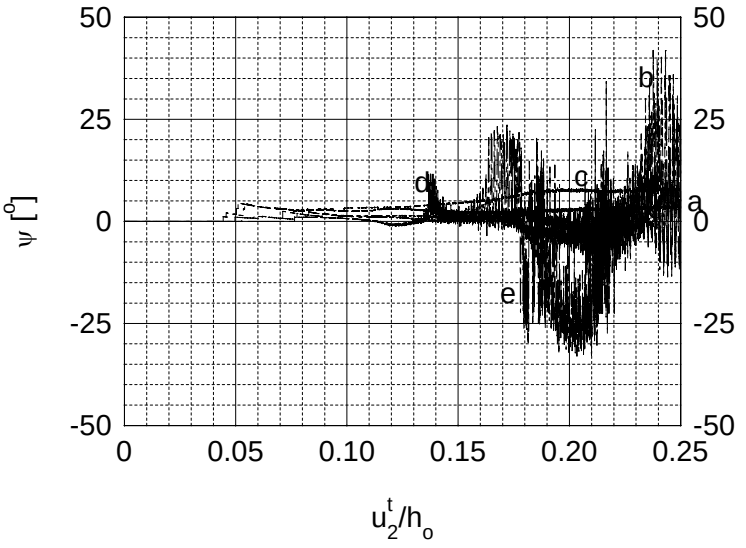

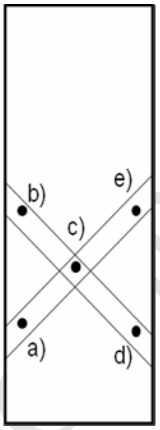

d)

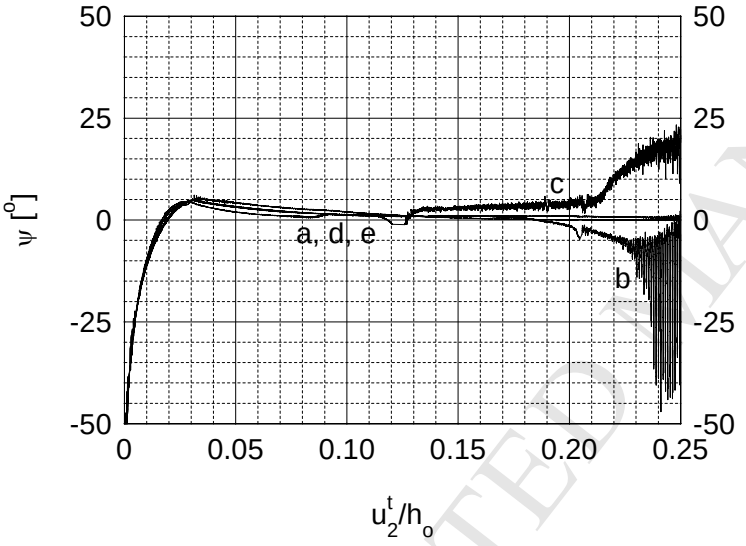

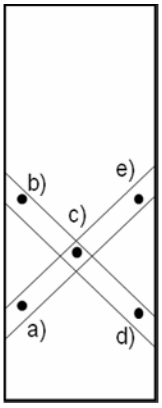

e)

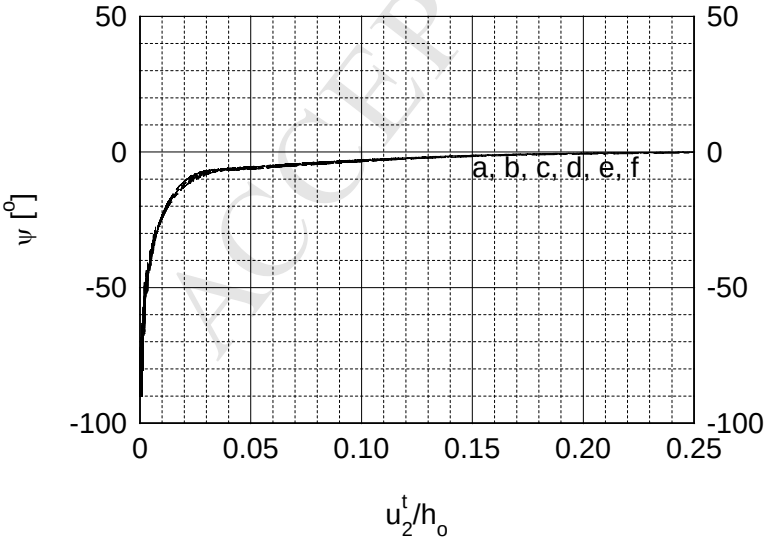

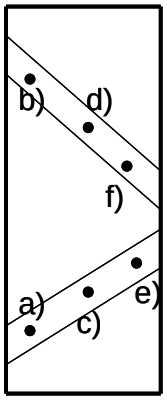

f)

FIGURE 5

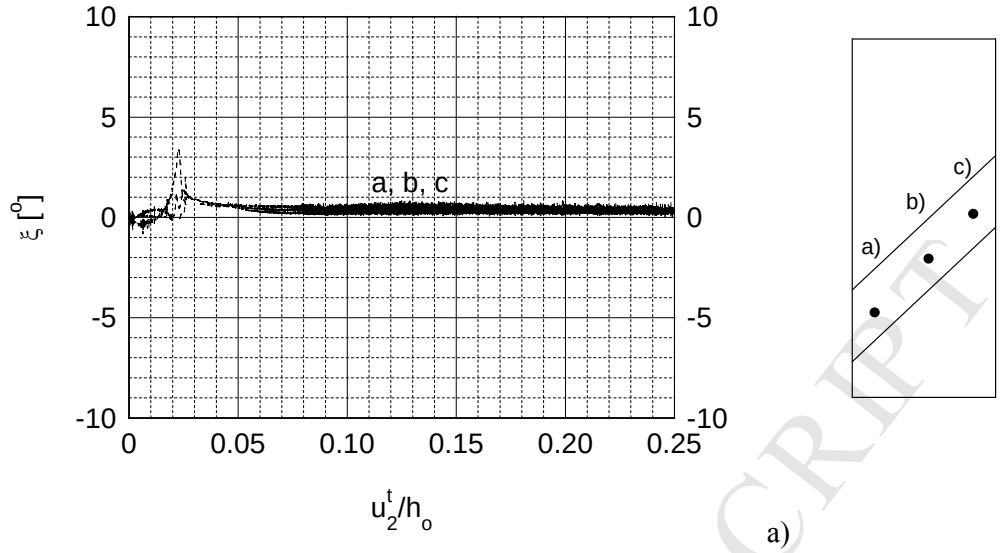

a)

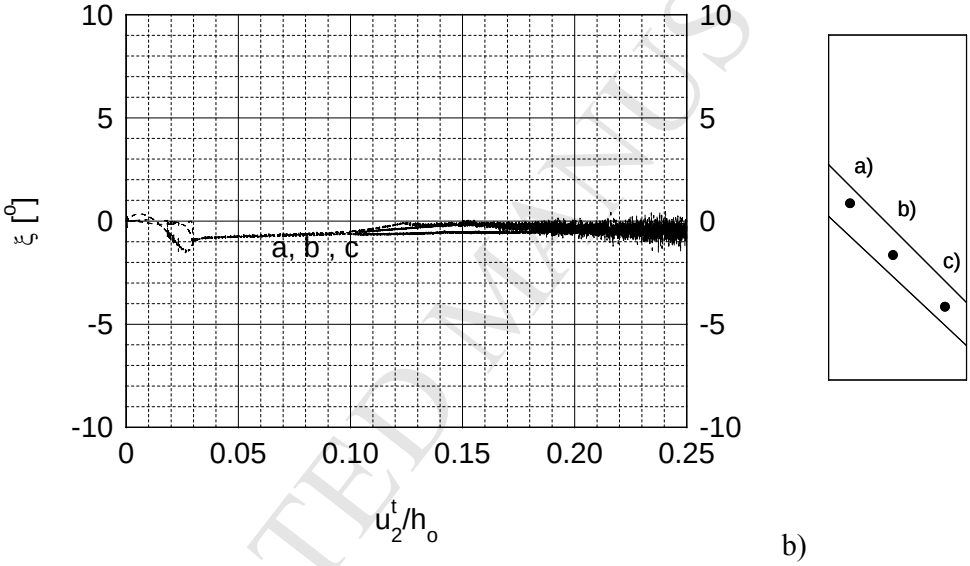

b)

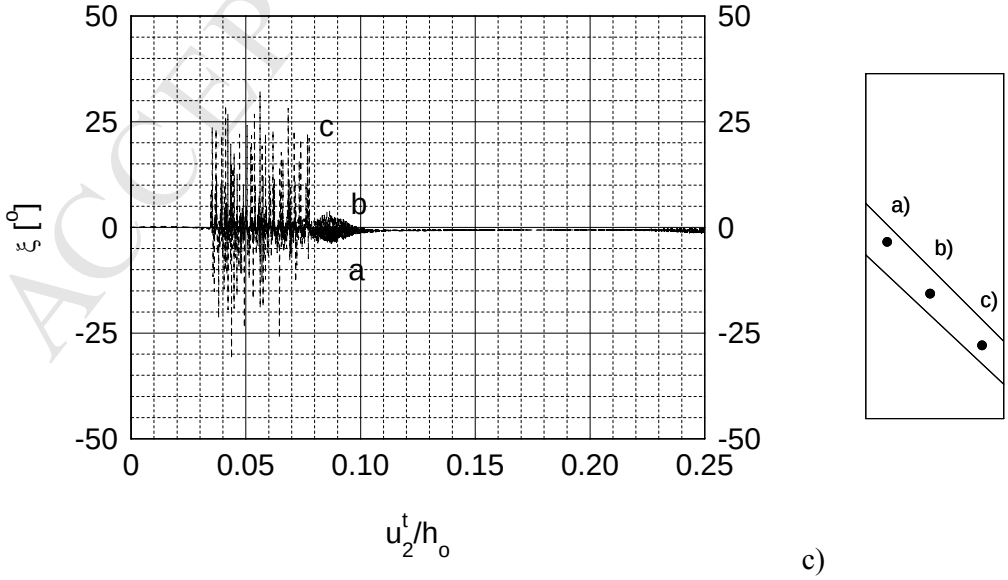

c)

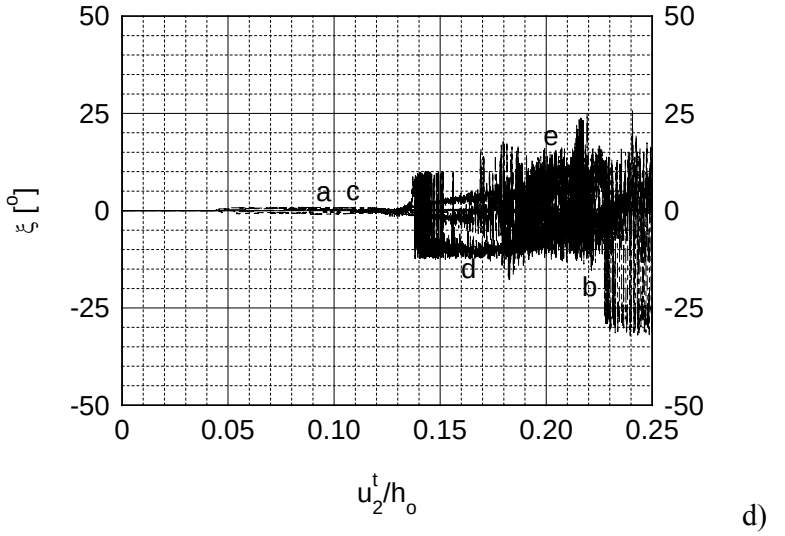

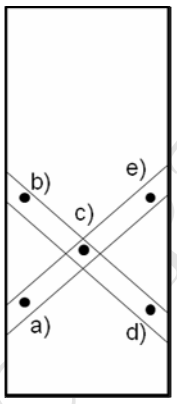

d)

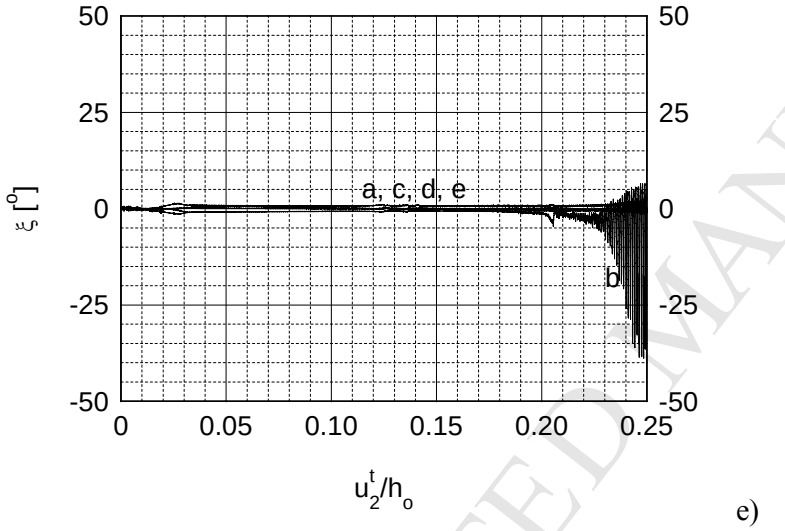

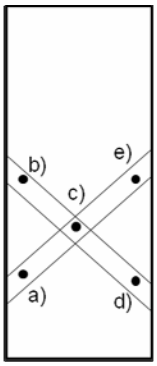

e)

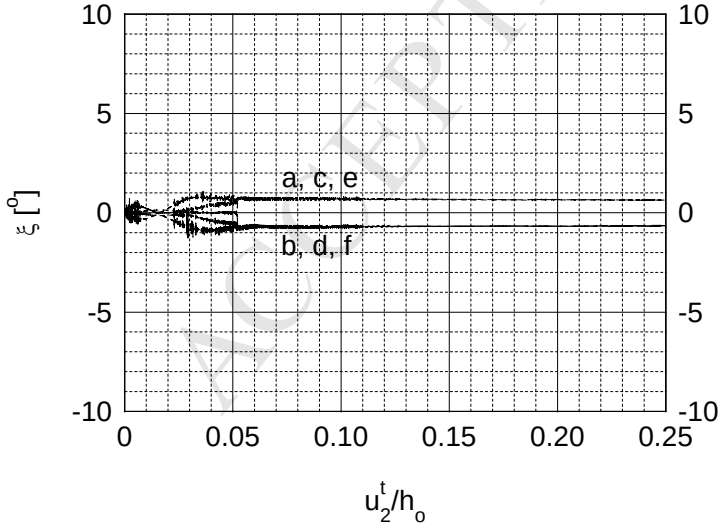

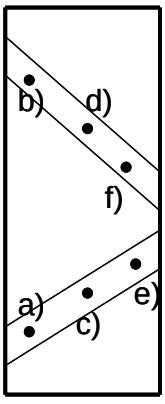

f)

FIGURE 6

Tab.1

Sand type	ψ (Eq.10)	ψ (Eq.11)	ψ (Eq.12)	ψ (FE analysis)
initially dense sand (e_o=0.55) (ϕ_{cx}=40°, ϕ=51.5°, ξ=1°)	8.1°	19.3°	20.4°	20°
initially medium dense sand (e_o=0.70) (ϕ_{cx}=36°, ϕ=38°, ξ=1°)	1.7	2.8°	3.2°	5°